Chinese Journal of Chemical Engineering 95 (2026) 162–174

Contents lists available at ScienceDirect

Chinese Journal of Chemical Engineering

journal homepage: www.elsevier.com/locate/CJChE

Full Length Article

Semi-hydrogenation of acetylene on Ni/H-zeolite catalysts with different zeolite topologies

Tong Guan [1], Xueming Sun [1], Rongbin Zhang [1], Huaxi Li [2,*], Gang Feng [1,3,*], Runping Ye [1,*]

[1] Key Laboratory of Jiangxi Province for Environment and Energy Catalysis, Institute of Applied Chemistry, School of Chemistry and Chemical Engineering, Nanchang University, Nanchang 330031, China
[2] Jiangxi Academy of Emergency Management Science, Nanchang 330031, China
[3] School of Textile and Clothing, Nantong University, Nantong 226019, China

ARTICLE INFO

Article history:
Received 1 November 2025
Received in revised form
11 January 2026
Accepted 16 January 2026
Available online 18 February 2026

Keywords:
Hydrocarbons
Hydrogenation
Zeolite
Topology
Catalyst

ABSTRACT

Zeolites are widely used in acetylene semi-hydrogenation to ethylene reaction due to their tunable acidity and ordered crystal porous structure. In this work, zeolites with different structures, including MTW, MFI, BEA, AEL, and MOR, were synthesized and impregnated with Ni. Characterization and performance evaluation of the catalysts were conducted for the acetylene semi-hydrogenation reaction. It was found that all catalysts had a high acetylene conversion rate. The Ni/H-Beta catalyst exhibited excellent catalytic performance at 150 °C achieving a 100% acetylene conversion rate and a 58% ethylene yield. The catalyst with BEA topology had the best performance. The results showed that Ni/H-Beta catalysts had large specific surface area and suitable microporous-mesoporous structure facilitate the formation of highly dispersed nickel species with fine particle sizes, and Beta zeolites had a larger proportion of medium and strong Lewis acid sites, which could effectively modify the electronic structure of Ni. This work investigated the efficacy of Ni catalysts supported on zeolites with different topologies for the semi-hydrogenation of high-concentration acetylene.
© 2026 The Chemical Industry and Engineering Society of China, and Chemical Industry Press Co., Ltd. All rights are reserved, including those for text and data mining, AI training, and similar technologies.

1. Introduction

As a cornerstone of the modern chemical industry, ethylene is a critical precursor for manufacturing various commodities, including polymers, solvents, and fine chemicals [1,2]. With the development of industry, the demand for ethylene is increasing [3,4]. At present, the production route of ethylene is mainly naphtha cracking and light hydrocarbon steam cracking [5,6], which is a burden for countries with oil shortages [7], so exploring non-petrochemical routes for ethylene production has greater research value and application prospects [8,9]. In coal resource-rich countries, research and development of coal chemical route to ethylene is necessary [10,11], which is mainly concentrated in two routes: “Coal to methanol then to ethylene” [12,13] and “Coal to acetylene then to ethylene” [14,15]. In recent years, despite the growing economic feasibility of the “coal to acetylene then to ethylene” route, driven by developments in calcium carbide acetylene production [16,17], the selective hydrogenation of high-concentration acetylene streams to ethylene with high efficiency and selectivity remains a critical impediment for industrial application [18].

Supports play a vital role in heterogeneous catalysis [19]. Conventional materials such as Al_2O_3 are commonly employed as supports in industrial applications. However, zeolites have received more and more attention in catalytic reaction due to their tunable acidity and ordered crystalline porous structure [20,21]. Sahooli *et al.*[22] explored Ce, Ir, Ag, and Pd modified Beta zeolites (BEA topology). Their findings identified that the incorporation of 0.29% Ir and 0.08% Pd yielded the most active and stable catalyst. Wang *et al.*[23] compared Ni catalysts loaded with different materials, such as SiO_2, γ-Al_2O_3, and ZSM-12 (MTW topology), and found that Ni/H-ZSM-12 catalysts had the best catalytic performance for the semi-hydrogenation of acetylene and introduction of Sn into the Ni/H-ZSM-12 catalysts can further improve the

* Corresponding authors.
E-mail addresses: lihxjxak@163.com (H. Li), fenggang@ntu.edu.cn (G. Feng), rye@ncu.edu.cn (R. Ye).

https://doi.org/10.1016/j.cjche.2026.01.009
1004-9541/© 2026 The Chemical Industry and Engineering Society of China, and Chemical Industry Press Co., Ltd. All rights are reserved, including those for text and data mining, AI training, and similar technologies.

ethylene selectivity and stability of the catalysts. Through *in situ* encapsulation, Liu *et al.*[24] constructed isolated Pd centers within a ZSM-5 matrix with high Al/Si content. The resulting catalyst exhibited remarkable performance in alkyne semi-hydrogenation, significantly lowering the reaction energy barrier while maintaining high styrene selectivity. Shi *et al.*[25] synthesized a series of organic amine-modified MOR zeolites (MOR topology) *via* ion exchange. By precisely introducing functional organic groups into MOR's pore channels as organic molecular gates, they substantially impeded the adsorption affinity and diffusion of C_2H_4. This significantly enhanced the adsorption selectivity of O-MOR towards CO_2 and C_2H_2 relative to C_2H_4, effectively removing CO_2 and C_2H_2 from C_2H_4 . The zeolite catalysts of SAPO-11 (AEL topology) were also investigated, which were shown to have high activity and selectivity [26,27]. Previous investigations into nickel-based acetylene hydrogenation catalysts have predominantly centred on conventional oxide supports or standalone zeolites supports [23,28,29], lacking systematic comparisons of zeolites with diverse topological structures. This limitation hinders the identification of universal principles governing how topology modulates reaction pathways through spatial confinement effects. Consequently, there remains a compelling need to investigate zeolite catalysts utilizing diverse topological frameworks [30,31]. This study systematically compares five zeolite supports with distinct topologies—MTW, MFI, BEA, MOR, and AEL—within a unified framework. By integrating *in-situ* DRIFTS, H_2-TPR, XPS, TEM, NH_3-TPD, Py-FTIR, BET and catalyst performance characterization, we discuss the structure-performance relationship of catalysts, revealing key mechanisms: confinement effects and synergistic interactions between acid sites and nickel sites.

Owing to its remarkable hydrogenation activity and favorable cost-effectiveness, nickel has been widely recognized as a promising catalytic metal [29,32,33]. It has been extensively employed in various hydrogenation processes, with significant research attention devoted to its application in acetylene hydrogenation [34]. In this study, we selected a series of H-type zeolites with distinct topological structures as supports. A series of zeolite catalysts were prepared by impregnating Ni and applied to the hydrogenation of acetylene to ethylene. This choice was based on the pivotal role of acid sites provided by H-type zeolites in the selective hydrogenation of acetylene [35]. H-zeolites possess both Brønsted and Lewis acid sites and are readily amenable to modification of their surface acid sites [36]. These acidic sites not only preferentially adsorb and activate acetylene molecules but also modulate the electron density of the active metal through metal-support interactions. The effects of zeolite topology on the properties, dispersion and reducibility of Ni species as well as the acetylene hydrogenation to ethylene reaction were investigated. Among these, the BEA topology exhibited the most favorable catalytic performance, simultaneously forming uniformly dispersed Ni^0 sites and moderately strong Lewis acid sites. These sites effectively modified the electronic structure of nickel, thereby promoting ethylene desorption.

2. Experimental

2.1. Catalyst preparation

A series of Ni/H-zeolite catalysts were prepared in two steps. The H-zeolite supports (H-ZSM-12, H-ZSM-5, H-Beta, H-MOR, H-SAPO-11) were synthesized *via* a hydrothermal procedure detailed in the Supplementary Material. These supports were then impregnated with an aqueous $Ni(NO_3)_2$ solution to achieve a nominal 2%(mass) Ni loading. Following drying at 80 °C for 10 h, the samples were calcined in air at 500 °C for 2 h, yielding the final catalysts.

2.2. Catalyst characterization

The detailed procedures for catalyst characterization are presented in the Supplementary Material (**Section S2** and Table S1).

2.3. Catalytic performance evaluation

The catalytic performance of the system's catalyst for acetylene semi-hydrogenation was evaluated in a fixed-bed reactor. Gas flow rates were precisely controlled by mass flow controllers. The catalyst (100 mg) was loaded into a glass tube and secured at both ends with a small amount of quartz wool. The catalyst was pre-reduced in flowing H_2 at 500 °C for 2 h prior to the reaction and subsequently cooled to ambient temperature. C_2H_2 (5 $ml \cdot min^{-1}$) and H_2 (10 $ml \cdot min^{-1}$) were introduced into the reactor with a gas hourly space velocity (GHSV) of 9000 $ml \cdot g^{-1} \cdot h^{-1}$. The temperature was raised from 50 °C to 250 °C in 25 °C increments. The outlet gas was automatically sampled *via* a six-port valve and analyzed online by GC. The analysis employed a Fuli 9790II gas chromatograph manufactured by Zhejiang Fuli Analytical Instrument Co., Ltd., utilizing the Haohan 790 gas chromatography system equipped with a TCD detector. The carrier gas was hydrogen, operated in constant flow mode. The temperature programme commenced at an initial temperature of 50 °C, ascended to 135 °C, and maintained this temperature for 5 min. The total component content within the reaction outlet gas stream was analyzed using the calibrated area normalization method.

C_2H_2 conversion ($X_{C_2H_2}$), C_2H_4 selectivity ($S_{C_2H_4}$), and C_2H_4 yield ($Y_{C_2H_4}$) are calculated as follows:

$$X_{C_2H_2} = \frac{[C_2H_2]_{in} - [C_2H_2]_{out}}{[C_2H_2]_{in}} \times 100\% \quad (1)$$

$$S_{C_2H_4} = \frac{[C_2H_4]_{out}}{[C_2H_2]_{in} - [C_2H_2]_{out}} \times 100\% \quad (2)$$

$$Y_{C_2H_4} = X_{C_2H_2} \times S_{C_2H_4} \times 100\% \quad (3)$$

$[C_2H_2]_{in}$ represents the feedstock concentration of acetylene, and $[C_2H_2]_{out}$ represents the acetylene concentration in the reactor effluent at a specified reaction temperature. Additionally, $[C_2H_4]_{out}$ represents the ethylene concentration in the reactor effluent at the same reaction temperature.

3. Results and Discussion

3.1. Catalyst characterization

3.1.1. XRD

The crystalline structure and phase purity of the synthesized zeolites were determined by X-ray diffraction (XRD). As shown in Fig. 1(a), the XRD patterns of H-ZSM-12 (MTW), H-ZSM-5 (MFI), H-Beta (BEA), H-MOR (MOR), and H-SAPO-11 (AEL) all displayed distinct diffraction features corresponding to their respective theoretical frameworks, confirming the successful preparation of phase-pure materials with the intended topological structures. The sharp diffraction peaks observed for each sample indicated high crystallinity and structural integrity. Following the impregnation with nickel (Fig. 1(b)), the XRD patterns maintained all the characteristic reflections of the parent zeolites, while no detectable diffraction signals corresponding to crystalline NiO phases were observed. This absence of NiO-related diffraction features

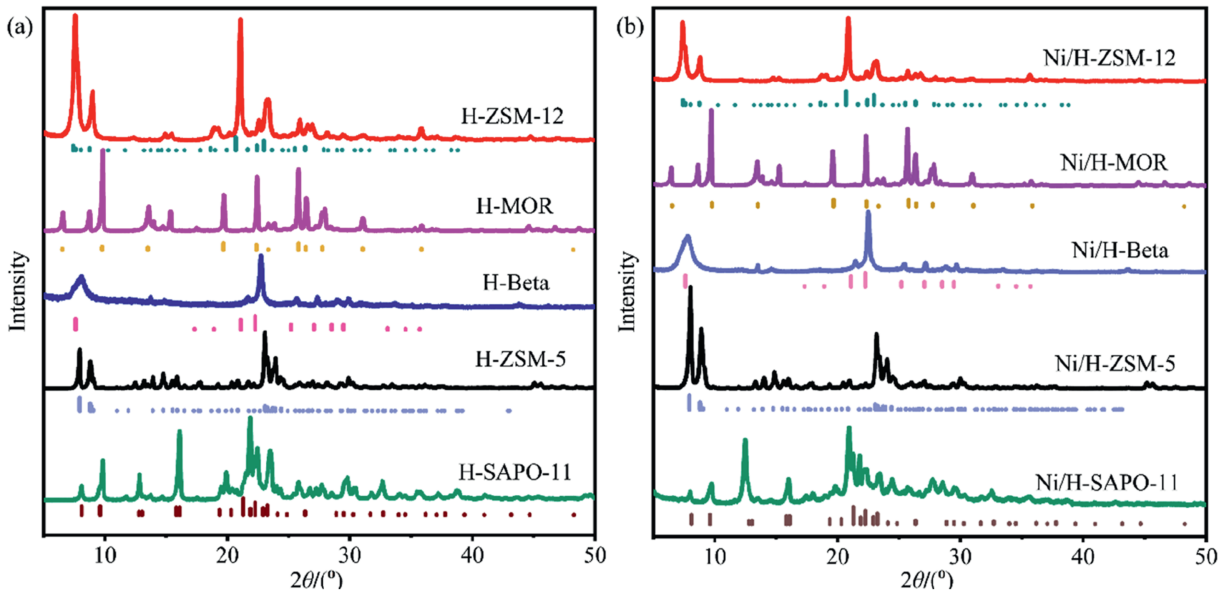


Fig. 1. (a) XRD patterns of the zeolites, (b) XRD patterns of the Ni/H-zeolite catalysts.

confirms that the active metal species, at the applied loading, exist as highly dispersed nanoparticles or clusters below the detection limit of XRD. Furthermore, the preservation of the zeolite diffraction patterns without significant loss in intensity or emergence of new phases demonstrates that the impregnation and subsequent calcination procedures did not alter or degrade the crystalline frameworks of the support materials.

3.1.2. BET

N_2 adsorption-desorption measurements were performed to evaluate the textural properties of zeolites with different topologies. As shown in Fig. 2(a) and (b), the N_2-adsorption and desorption curves of Ni/H-ZSM-5, Ni/H-SAPO-11, and Ni/H-ZSM-12 catalysts are all isotherms of type IV, with hysteresis lines of type H4, which indicate that they have both microporous and mesoporous structures. The N_2 adsorption-desorption isotherms of Ni/H-Beta and Ni/H-MOR catalysts were of type I, and the adsorption and desorption curves basically overlapped, indicating that the Ni/H-Beta and Ni/H-MOR catalysts were dominated by microporous structures. The corresponding specific surface area (S_{BET}), pore volume (V_P), and average pore diameter (D_P) are summarized in Table 1. It can be seen that the specific surface area of the five catalysts was ranked as Ni/H-Beta > Ni/H-MOR > Ni/H-ZSM-5>Ni/H-ZSM-12>Ni/H-SAPO-11. The substantially larger surface area of the BEA and MOR topology-based catalysts implies a greater capacity for hosting active sites, which is beneficial for the acetylene hydrogenation reaction. Considering the combined effects of micropore and mesopore volumes alongside its performance characteristics, it can be concluded that a higher mesopore volume facilitates greater acetylene conversion rates at lower

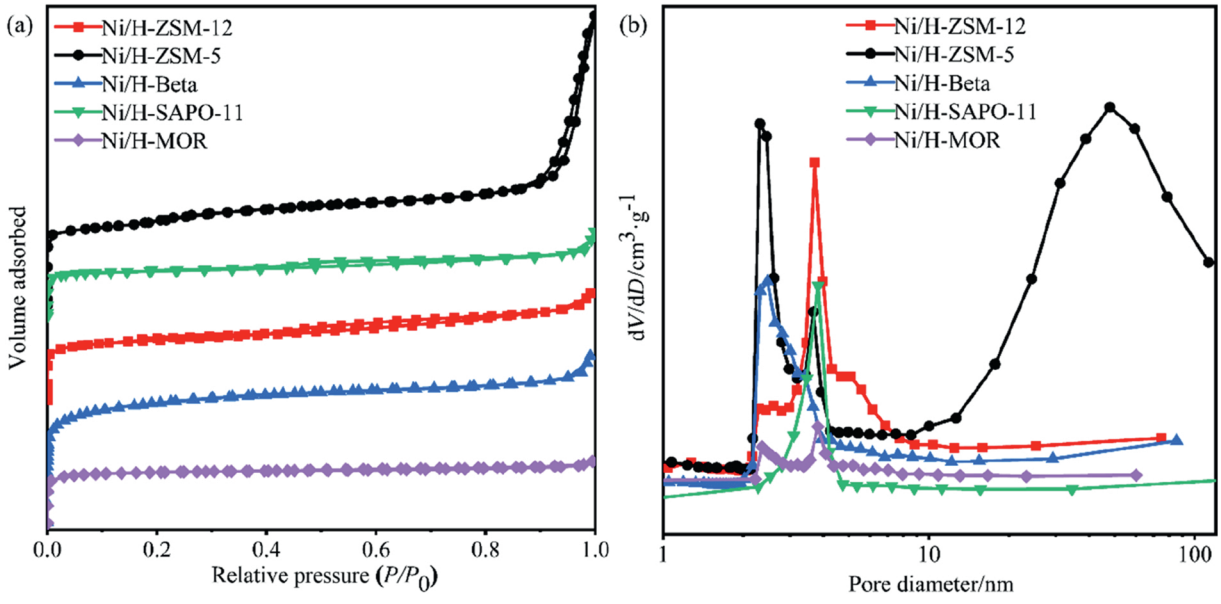


Fig. 2. (a) N_2 adsorption and desorption isotherms of Ni/H-zeolite catalysts, (b) Pore size distribution curves obtained from BJH calculations.

Table 1
Physicochemical properties of prepared samples.

Samples	S_{BET}/m^2·g	V_{meso}/cm^3·g	V_{micro}/cm^3·g	D_p/nm	Ni loading /% (mass)	Si/Al (atomic)
Ni/H-ZSM-12	235	0.104	0.104	2.71	2.28	57.76
Ni/H-ZSM-5	313	0.371	0.143	5.47	2.34	26.41
Ni/H-Beta	554	0.098	0.112	2.38	2.39	43.41
Ni/H-SAPO-11	205	0.079	0.060	3.26	1.97	0.13
Ni/H-MOR	474	0.021	0.177	2.38	2.23	14.88

temperatures. For instance, Ni/H-ZSM-12 and Ni/H-ZSM-5 exhibit elevated acetylene conversion rates at low temperatures. Microporous volume correlates with catalyst selectivity; for instance, Ni/H-MOR exhibits high ethylene selectivity due to its dominant microporous volume. Crucially, our data indicate that optimal catalytic performance depends not on maximising any single pore volume type, but on achieving a balanced synergy between them [37–39]. For example, the Ni/H-Beta catalyst possesses moderate mesoporous and microporous volumes, delivering overall favorable catalytic performance.

Additionally, ICP-OES analysis confirmed that the actual Ni loadings of all catalysts were in close agreement with the theoretical values (Table 1), verifying the accuracy of the impregnation process. Analysis of the Si and Al elemental composition in the catalysts *via* XRF revealed that the actual Si/Al atomic ratios for all catalysts, which are matched with the theoretical values, thereby validating the accuracy of the zeolite support synthesis (Table 1).

3.1.3. SEM and TEM analysis

To gain a deeper understanding of the structural characteristics of Ni supported on zeolites with different topologies and to explore the influence of the zeolite structure, the samples were analyzed using SEM. In addition, TEM and HRTEM analyses were performed on Ni/H-Beta and Ni/H-ZSM-12 samples. The SEM results showed that Ni/H-ZSM-12 catalysts presented a relatively regular cubic structure (Fig. 3(a)), Ni/H-ZSM-5 catalysts presented a cubic structure with smaller dimensions (Fig. 3(b)), Ni/H-MOR catalysts presented an elliptical shape with uniform dimensions and a well-defined lamellar structure (Fig. 3(c)), Ni/H-Beta catalyst presents a round sphere shape (Fig. 3(d)), and Ni/H-SAPO-11 catalyst presents an elliptical sphere shape (Fig. 3(e)). SEM characterization showed that none of the five catalysts had obvious agglomeration.

TEM results further illustrated the differences between Ni/H-Beta catalyst and Ni/H-ZSM-12 catalyst. Fig. 4(b) shows the HRTEM image of Ni/H-Beta catalyst, and lattice fringes of 0.201 nm and 0.202 nm belonging to the (1 1 1) crystalline plane of Ni were detected, which proved that Ni was successfully introduced into the Beta support. Fig. 4(c) shows that the HRTEM image of the Ni/H-ZSM-12 catalyst is similar to that of the Ni/H-Beta catalyst, and the appearance of lattice fringes with a spacing of 0.201 nm and 0.203 nm attributed to the (1 1 1) crystalline plane of Ni proves the successful introduction of Ni into the ZSM-12 support. As shown by the EDS elemental mapping analysis (Fig. 4(c) and (f)), Ni was more uniformly dispersed on the Beta support than on the ZSM-12 support. A particle size analysis of nickel particles across five catalysts (Fig. 4 and Fig. S1) revealed smaller nickel particle dimensions within the Ni/H-Beta catalyst. Within zeolites featuring the BEA topology, nickel particles were finer and more dispersed. This dispersion likely provided more active sites for the hydrogenation of acetylene to ethylene. Furthermore, the minute particle size of metallic nickel reduced excess hydrogenation and promoted ethylene desorption [28].

3.1.4. NH_3-TPD and Py-FTIR analysis

To study the acidity of zeolites with different topologies, NH_3-TPD and Py-FTIR characterization were performed. The signal peaks at around 200 °C were attributed to weakly acidic sites, those at 250–350 °C to medium-strongly acidic sites, and those at 350–500 °C to strongly acidic sites [40,41]. Ni/H-ZSM-5, Ni/H-SAPO-11 and Ni/H-ZSM-12 catalysts only have one signal peak at 220 °C (Fig. 5(a)), indicating the presence of only weakly acidic sites in Ni/H-ZSM-5, Ni/H-SAPO-11 and Ni/H-ZSM-12. Ni/H-Beta catalysts only have one signal peak at 260 °C, indicating the presence of only moderately strong acidic sites in Ni/H-Beta. The Ni/H-MOR catalyst only has one signal peak at 420 °C, indicating that only strong acidic sites exist in Ni/H-MOR. The NH_3-TPD results for all samples in Fig. 5(a) have been integrated and compiled in Table 2, where the total acid amount of Ni/H-MOR is designed as 1. These results have been cross-validated with Py-FTIR test results in terms of magnitude and trend.

The acid properties of the Ni-supported zeolite catalysts were analyzed in detail by pyridine-adsorption FTIR (Py-FTIR). As shown in Fig. 5, and Fig. S2, all samples exhibited five characteristic vibrational bands in the region of pyridine adsorption: near 1445–1448 cm^{-1}, assigned to Lewis acid sites (L acid); near 1540–1543 cm^{-1}, attributed to Brønsted acid sites (B acid); and around 1490–1492 cm^{-1}, associated with combined B and L acid sites [42]. These spectral features confirm the co-existence of both Brønsted and Lewis acidity in all catalysts.

According to the quantitative results summarized in Table 2, Ni/H-Beta showed the highest total acid density among the five catalysts, along with the most abundant population of Lewis acid sites. In contrast, the acid site concentrations of the remaining four catalysts are relatively low, particularly in terms of Lewis acidity, a conclusion further validated by NH_3-TPD analysis (Fig. 5(a) and Table 2). Combining Table 2 and catalytic performance leads to the conclusion that rich distribution of Brønsted and Lewis acid sites in Ni/H-Beta is considered beneficial for facilitating the adsorption and activation of reactants, which may contribute to its superior catalytic performance in acetylene semi-hydrogenation.

3.1.5. H_2-TPR analysis

The reduction behavior and metal-support interaction of Ni supported on different zeolites were studied by H_2-TPR (Fig. 6(a)). The dual peaks observed in the spectrum arise from differing interactions between NiO and the carrier. The α peak in the low-temperature region corresponds to the reduction reaction of bulk NiO, which is more readily reduced due to the weak interaction between Ni species and the support. Conversely, the β peak in the high-temperature region corresponds to surface nickel silicate or NiO present as samll, difficult-to-reduce particles, requiring higher reduction temperatures due to the strong interaction between Ni species and the support [43–45]. The peaks in all five catalysts are attributed to the reduction of NiO material. It can be observed that the Ni/H-ZSM-12 catalyst exhibits the weakest strong metal-support interactions. The shift of the reduction peak towards higher temperatures indicates stronger

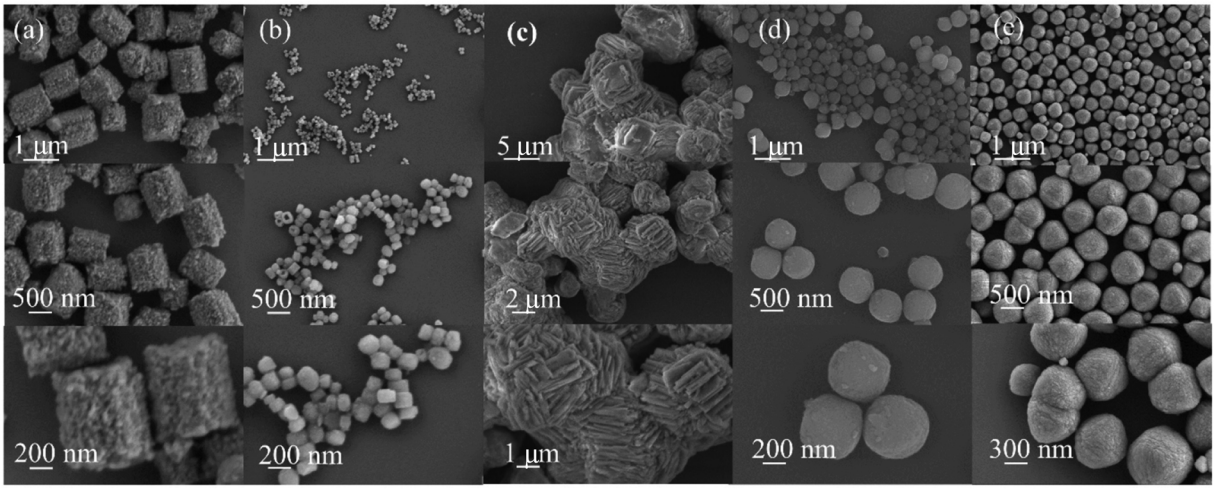


Fig. 3. SEM images of Ni/H-zeolite catalysts: (a) Ni/H-ZSM-12, (b) Ni/H-ZSM-5, (c) Ni/H-MOR, (d) Ni/H-Beta and (e) Ni/H-SAPO-11.

metal-support interactions, rendering the nickel species more difficult to reduce. By comparing peak areas (Table S3), it is evident that the Ni/H-Beta catalyst predominantly supports readily reducible NiO species, whereas the Ni/H-MOR catalyst primarily harbours NiO species that are difficult to reduce [45,46].

3.1.6. C_2H_4-TPD analysis

In order to investigate the adsorption and desorption characteristics of C_2H_4 on the surfaces of zeolites with different topologies, all catalysts were characterized by C_2H_4-TPD, as shown in Fig. 6(b). It is imperative that ethylene, as the target product, undergoes fast desorption from the catalyst to avoid further reactions such as over-hydrogenation to ethane or oligomerization [47]. Consequently, the weak adsorption of ethylene on active sites is paramount for attaining high selectivity. C_2H_4-TPD profiles revealed two main desorption peaks for the series of catalysts, indicative of two distinct types of adsorbed ethylene species. The peaks around 200 °C were attributed to the weak π-bonded ethylene desorption peaks [48], with the largest area of the weak π-bonded ethylene desorption peaks on Ni/H-Beta catalysts, and the lowest temperature of the weak π-bonded ethylene desorption peaks on Ni/H-ZSM-12 catalysts, indicating that weak π-bonded ethylene desorption was the largest on Ni/H-Beta catalysts. The weak π-bond ethylene desorption peaks on Ni/H-Beta catalysts are broad peaks, which may be attributed to the inhomogeneity of the energy distribution of the adsorption sites on the catalysts. The peaks above 350 °C are attributed to the strong di-σ ethylene desorption peaks [49,50], and the maximum area of high-temperature peaks is found on Ni/H-MOR catalysts. The C_2H_4-TPD results for all samples in Fig. 6(b) have been integrated and included in Table S4, with the low-temperature ethylene desorption yield of Ni/H-ZSM-12 defined as 1. Table S4 indicates that the Ni/H-Beta catalyst exhibits the largest weak π-bonded ethylene desorption peak under low-temperature conditions. This result aligns with its catalytic performance, suggesting that ethylene readily desorbs from the Ni/H-Beta surface at low temperatures.

3.1.7. In-situ DRIFTS analysis

In-situ DRIFTS was carried out to investigate the catalytic reaction mechanism of the following five catalysts, and the adsorption, conversion, and desorption processes of different species on Ni/H-Beta and Ni/H-ZSM-12 were investigated at 150 °C. This work focused on unraveling the fundamental reaction pathways and active-site interactions governing the selective hydrogenation of acetylene to ethylene. *In-situ* DRIFTS were used to observe the adsorption of reactants, products and intermediates on the surfaces of different catalysts. Consistent with earlier vibrational studies [51–53], the adsorption and reaction of C_2H_2 and C_2H_4 on metal catalysts can yield a wide array of surface hydrocarbon fragments, including π- and σ-bonded C_2H_2 and C_2H_4, as well as various C_2 species. Consequently, the vibrational assignment for the spectra presented in Fig. 7 and Fig. S3, which tracks C_2H_2 hydrogenation on the following five catalysts at different temperatures, proves to be highly complex.

The vibrational peaks of the ν(≡C—H) pyrolyzed material adsorbed on the catalyst surface by gaseous C_2H_2 are located at 3315, 3267, and 730 cm^{-1}. The vibrational peaks of ethyl intermediates produced during C_2H_2 hydrogenation are located at 2962, 2878 cm^{-1}. *In-situ* DRIFTS analyses show the presence of σ-bonded $^*CH{=}CH_2$ (1586 cm^{-1}) and π-bonded $CH_2{=}CH_2$ (2931, 1667 cm^{-1}) [54,55]. In exploring the complex correlation between catalyst performance and the behavior of the reaction intermediates, changes in the vibrational peaks of C_2H_4 (C_2H_4 adsorbed), which is the key intermediate, reveal the catalytic process kinetics and product selectivity. Specifically, changes in the intensity of the vibrational peaks of C_2H_4 reveal the ease of desorption of ethylene molecules from the catalyst surface, which profoundly affects the pathway and efficiency of the catalytic reaction. When the vibrational peak of C_2H_4 is significantly enhanced, it indicates that the desorption process of ethylene molecules encounters a larger energy barrier, which increases their residence time on the catalyst surface. The above limiting effect in turn, affects the selectivity of the whole catalytic system.

Combining the results of the *in-situ* DRIFTS tests of the five catalysts, it can be seen that the C_2H_3 peak of the Ni/H-MOR catalyst is gradually enhanced with increasing reaction temperature, indicating the beginning of C_2H_2 conversion. At the same time, a very weak C_2H_4 appeared, which indicated that C_2H_3 tended to be further hydrogenated to C_2H_4. The intensity of the vibrational peak of C_2H_4 at 1667 cm^{-1} decreased with increasing reaction temperature, which indicated that the rate of desorption of C_2H_4 was greater than that of its generation, and the intensity of the vibrational peak of ν(≡C—H) was larger at 250 °C, which indicated that there was more unconverted acetylene at 250 °C, and the results correlated well with the catalytic performance

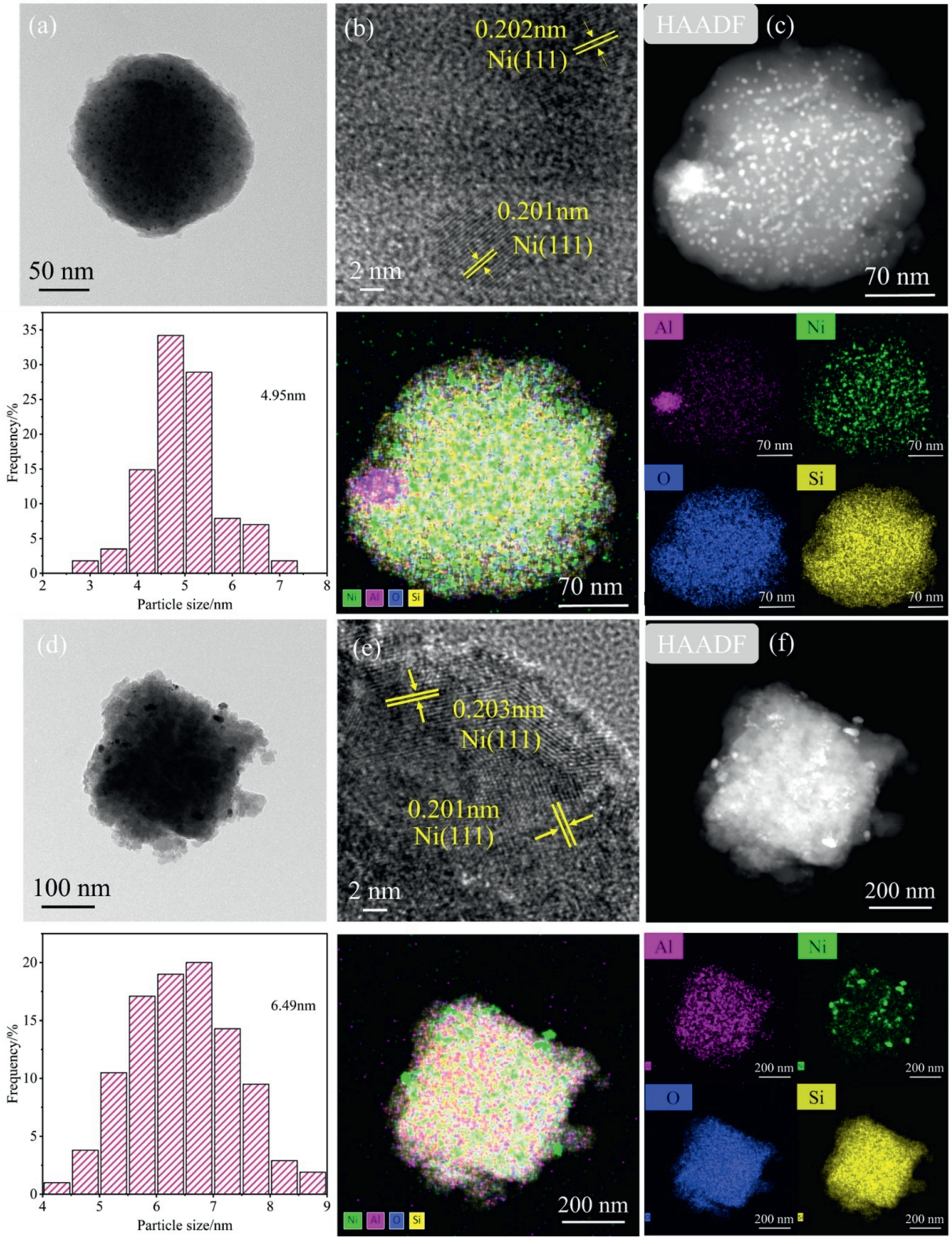


Fig. 4. (a) TEM image of Ni/H-Beta, (b) HRTEM image of Ni/H-Beta, (c) mapping image of Ni/H-Beta, (d) TEM image of Ni/H-ZSM-12, (e) HRTEM image of Ni/H-ZSM-12, (f) mapping image of Ni/H-ZSM-12.

(Fig. 7(a)), thus providing a rationale for the observed activity. The results are consistent with the catalytic results. For the Ni/H-ZSM-12 catalyst, C_2H_4 has the largest vibrational peak intensity at 2931 cm^{-1}, indicating that the desorption rate of C_2H_4 is the slowest on the Ni/H-ZSM-12 catalyst compared to the other two catalysts (Fig. 7(b)). The vibrational peak intensity of C_2H_4 at 2931 cm^{-1} on the Ni/H-Beta catalyst is relatively low, and the vibrational peak intensity of ν(≡C—H) is also diminished [56],

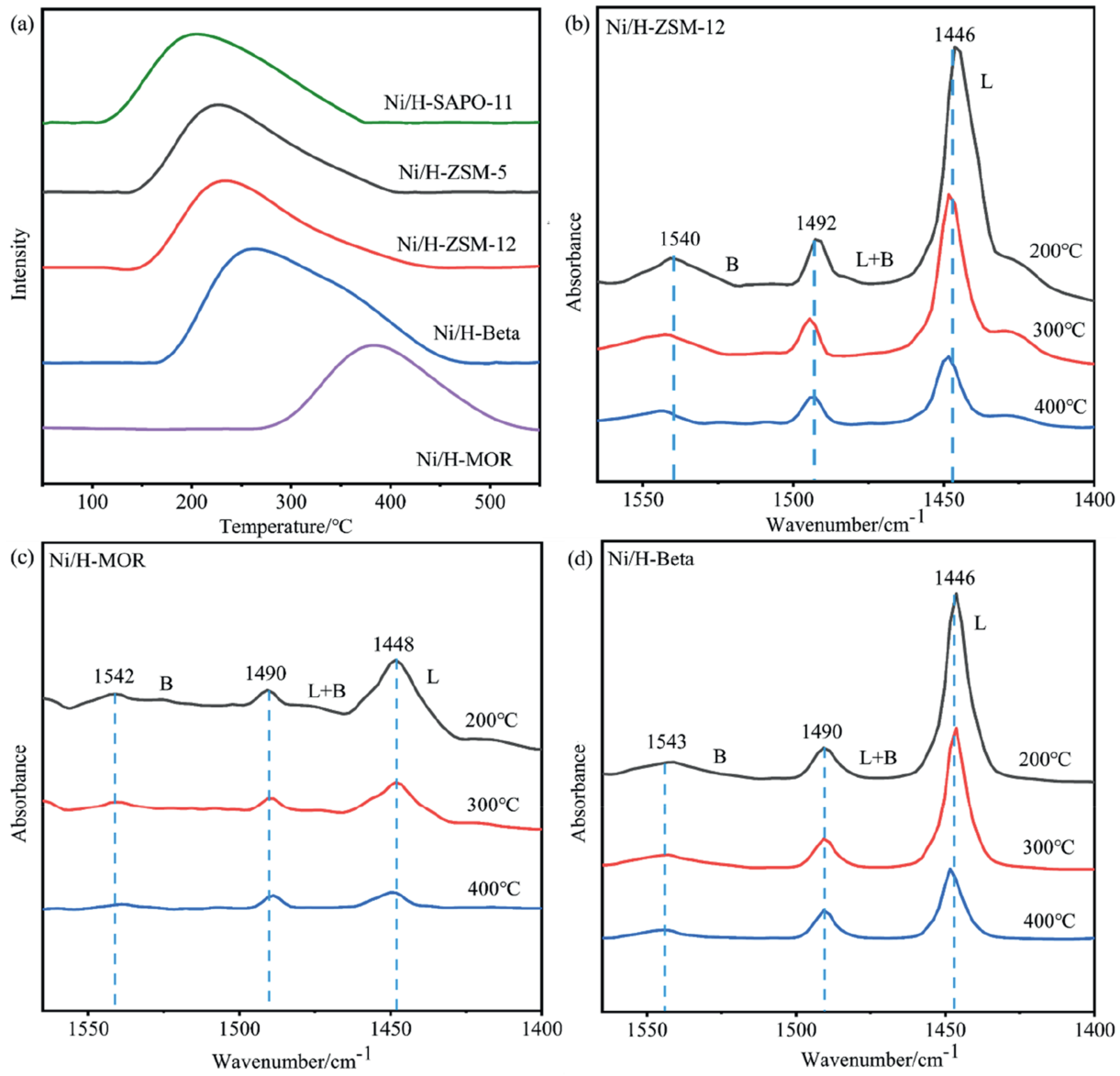


Fig. 5. (a) NH_3-TPD and (b) Py-FTIR spectra of Ni/H-zeolite catalysts.

Table 2
Statistics of Py-FTIR results for different catalysts.

Sample	Total acid amount	200 °C			300 °C			400 °C		
		B	L	L/B	B	L	L/B	B	L	L/B
Ni/H-ZSM-12	1.27	38.09	237.64	6.24	30.79	86.73	2.82	15.44	38.34	2.48
Ni/H-MOR	1.00	4.61	25.57	5.55	3.77	14.24	3.78	2.44	5.19	2.13
Ni/H-Beta	1.97	131.10	619.54	4.73	103.38	448.92	4.34	62.13	215.06	3.46
Ni/H-ZSM-5	1.28	36.58	151.40	4.14	24.20	73.96	3.05	13.16	24.46	1.86
Ni/H-SAPO-11	1.64	7.16	43.83	6.12	4.53	20.67	4.56	2.43	8.77	3.61

Note: The total acid amount of Ni/H-MOR was designed as 1; The amounts of B acid and L acid, expressed in units of $\mu mol \cdot g^{-1}$, were calculated using the Emeis coefficient method.

indicating that as the temperature increases, the conversion of C_2H_2 on the Ni/H-Beta catalyst is complete, and the desorption rate of C_2H_4 is rapid (Fig. 7(c)). On Ni/H-ZSM-5 and Ni/H-SAPO-11 catalysts, the intensity of the ν(≡C—H) vibration peak diminishes rapidly with increasing temperature, whilst the C_2H_4 vibration peak at 2931 cm^{-1} exhibits greater intensity (Fig. S3). This indicates that acetylene conversion proceeds more rapidly than ethylene desorption at elevated temperatures, consistent with performance testing results. The *in-situ* DRIFTS results for the five catalysts collectively indicate that at low temperatures, the Ni/H-Beta catalyst exhibits a higher acetylene conversion rate alongside superior ethylene selectivity.

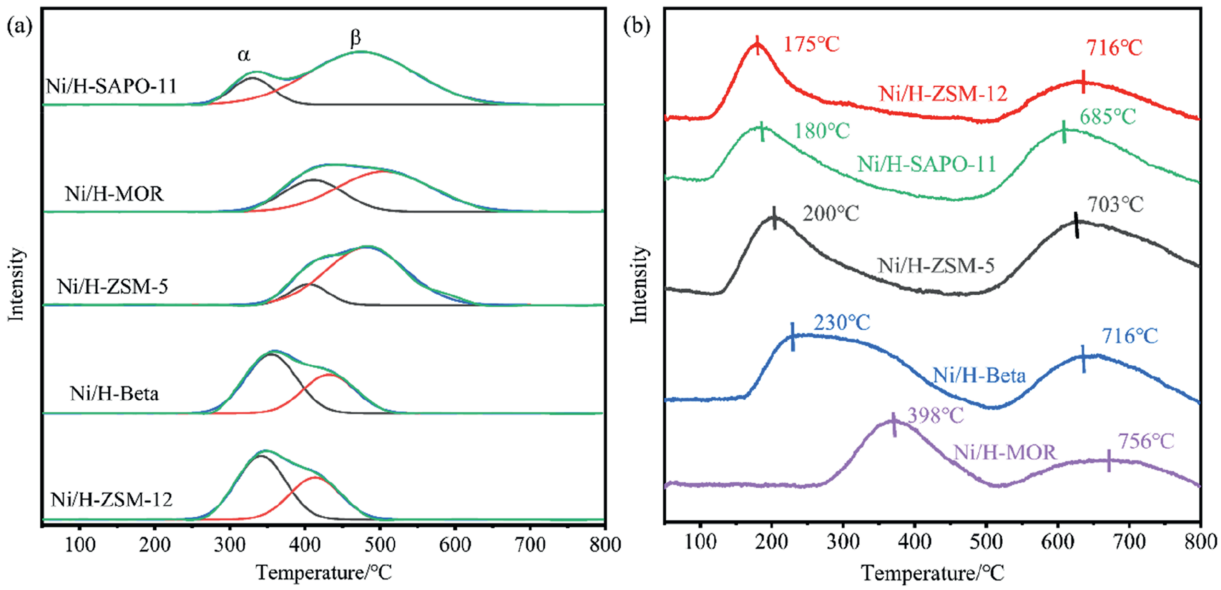


Fig. 6. (a) H_2-TPR and (b) C_2H_4-TPD curves of Ni/H-zeolite catalysts.

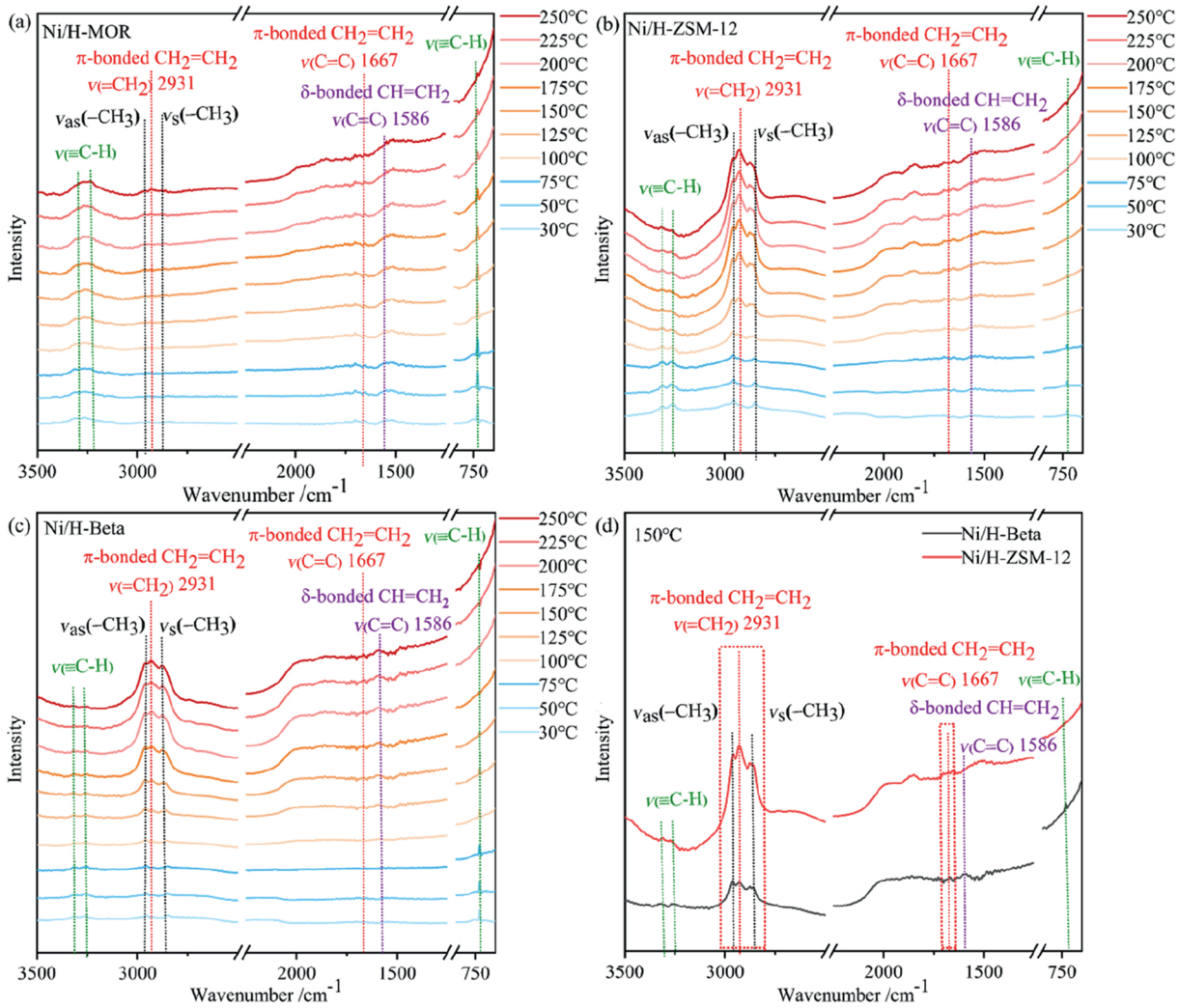


Fig. 7. *In-situ* DRIFTS spectra of acetylene hydrogenation reaction on the catalyst surface: (a) Ni/H-MOR, (b) Ni/H-ZSM-12, (c) Ni/H-Beta, (d) Comparison results of Ni/H-Beta and Ni/H-ZSM-12 catalysts at 150 °C.

In addition, Fig. 7(d) shows the changes of Ni/H-Beta and Ni/H-ZSM-12 catalysts during C_2H_2 semi-hydrogenation at 150 °C. The spectral peaks of the two catalysts exhibit similar signals, but there is a significant difference in intensity, especially for the peak intensity of C_2H_4. The peak intensity of C_2H_4 on Ni/H-Beta is weaker than that on Ni/H-ZSM-12, indicating that C_2H_4 adsorbed on Ni/H-Beta is more readily desorbed than C_2H_4 adsorbed on Ni/H-ZSM-12.

3.1.8. XPS analysis

XPS analysis of the catalyst surfaces was performed, with the results revealed in Fig. 8. All samples showed three signal peaks at Ni $2p_{3/2}$, with binding energies of 853.5 eV, 856.6 eV and 862.4 eV attributed to the Ni^0 peak, Ni^{2+} peak and Ni satellite peak [57]. The presence of Ni^{2+} is mainly due to the rapid oxidation of Ni^0 caused by air during the non-*in situ* measurement. The binding energy of Ni 2p exhibits shifts across different zeolite supports, providing direct evidence for variations in metal-support electron interactions. From Table 3, it can be seen that among the five catalysts the Ni^0 of Ni/H-Beta catalyst has the largest percentage, indicating that after the catalyst is pretreated with H_2, the NiO species are efficiently reduced to metal Ni^0, and the greater the density of metal Ni^0 sites on its surface that can be involved in the reaction, which may also be the reason for the more dispersed Ni substances in the TEM of Ni/H-Beta catalyst. Further comparing the binding energies of Ni^0 in the five catalysts, it can be seen that the binding energy of Ni^0 is the lowest in the Ni/H-Beta catalyst, indicating that Ni has gained more electrons, which may be because the Beta zeolite somehow facilitates the transfer of electrons from Al to Ni, or that the Beta zeolite itself forms a certain structure with Ni, which leads to an increase in the density of the electron cloud of Ni. The modulation of the electronic structure of Ni, characterized by increased charge density, serves as a key factor in promoting ethylene desorption and enhancing catalytic selectivity [58]. The Ni/H-MOR catalyst exhibits the lowest Ni^0 content and highest Ni^0 binding energy. The positive shift in binding energy unequivocally indicates that the Ni species exists in an electron-deficient state, which may characterize the strong metal-support interactions to Ni/H-MOR. The Ni species states in Ni/H-ZSM-5, Ni/H-ZSM-12 and Ni/H-SAPO-11 catalysts may be related to the pore-limiting effects of their respective supports. The Ni^0 content in Ni/H-ZSM-5, Ni/H-ZSM-12 and Ni/H-SAPO-11 catalysts lies at an intermediate value, consistent with the results from H_2-TPR analysis.

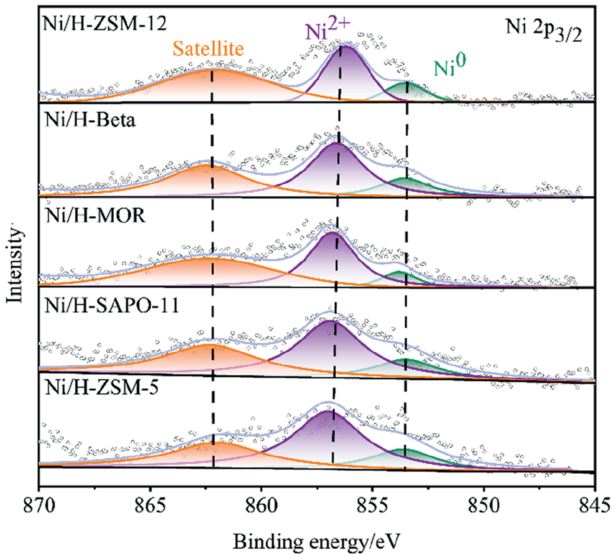


Fig. 8. XPS patterns of catalysts after reduction.

Table 3
XPS (Ni $2p_{3/2}$) analysis results of catalysts.

Sample	Binding energy/eV		Proportion/%
	Ni^0	Ni^{2+}	$Ni^0/(Ni^0+Ni^{2+})$
Ni/H-ZSM-12	853.7	856.2	24
Ni/H-Beta	853.5	856.6	26
Ni/H-MOR	854.2	856.8	19
Ni/H-SAPO-11	853.7	856.4	24
Ni/H-ZSM-5	853.6	857.0	25

3.2. Structure and performance of catalysts

3.2.1. Effect of different zeolite topologies on the catalytic performance

The catalytic performance of Ni supported on various zeolite topologies for acetylene hydrogenation is presented in Fig. 9. As shown in Fig. 9(a), the Ni/H-ZSM-12 catalyst has the best effect on acetylene conversion, and the complete conversion of acetylene can be realized at 125 °C. The Ni/H-MOR catalyst shows poor acetylene conversion performance, achieving complete acetylene conversion only at 175 °C, and the acetylene conversion rate decreases at 250 °C. Typically, the loss of catalytic activity can be attributed to the accumulation of metal agglomerates and carbonaceous coke deposits [59]. Thermal gravimetric analysis of the post-reaction catalysts (Fig. S4) revealed that the Ni/H-MOR catalyst exhibited superior resistance to coking compared to the other four catalysts, likely owing to its unique one-dimensional straight-channel structure. For the Ni/H-MOR catalyst synthesized *via* the impregnation method, deactivation is most likely attributable to minor agglomeration of nickel metal particles [59,60]. The Ni/H-Beta, Ni/H-ZSM-5 and Ni/H-SAPO-11 catalysts all achieved complete conversion of acetylene at 150 °C. However, due to the high activity of Ni/H-ZSM-12 catalyst, acetylene was over-hydrogenated to ethane at low temperatures. The selectivity and yield of ethylene gradually increased, but it was still lower than 50% (Fig. 9(c)). The Ni/H-MOR catalysts showed higher selectivity of ethylene under the complete conversion of acetylene, but there was a deactivation phenomenon at 250 °C (Fig. 9(b)). Ni/H-Beta exhibits high acetylene conversion rates and ethylene selectivity at temperatures above 150 °C. The catalytic performances of the catalysts at 150 °C are shown in Fig. 9(d), and the ethylene yields are as follows: Ni/H-Beta > Ni/H-ZSM-5>Ni/H-MOR > Ni/H-ZSM-12>Ni/H-SAPO-11. Overall, the Ni/H-Beta catalyst demonstrated superior performance, exhibiting optimal catalytic activity at 150 °C, which achieved 100% acetylene conversion and an ethylene yield of 58%. After reviewing multiple literature sources and comparing the acetylene hydrogenation catalytic performance of Ni/H-Beta with catalysts from published articles, the summary comparison is presented in Table S2. The results demonstrate that the catalytic performance of Ni/H-Beta surpasses that of certain catalysts based on MCM-41, S-1 zeolite supports, and Ni-loaded catalysts.

To evaluate the stability of the Ni/H-Beta catalyst in the C_2H_2 semi-hydrogenation reaction, stability testing was conducted at 150 °C. The stability test results are shown in Fig. S5. The stability test results indicate that the acetylene conversion rate reached 100%, with ethylene selectivity gradually increasing. After 4 h of testing, activity gradually declined. The catalyst mass increased from 0.1 g to 0.16 g during the stability test, a gain associated with the formation of green oil during the reaction. The thermogravimetric analysis curve (Fig. S6) indicates that mass loss between 100 °C and 300 °C for both post-stability-tested and freshly reduced samples is attributed to the

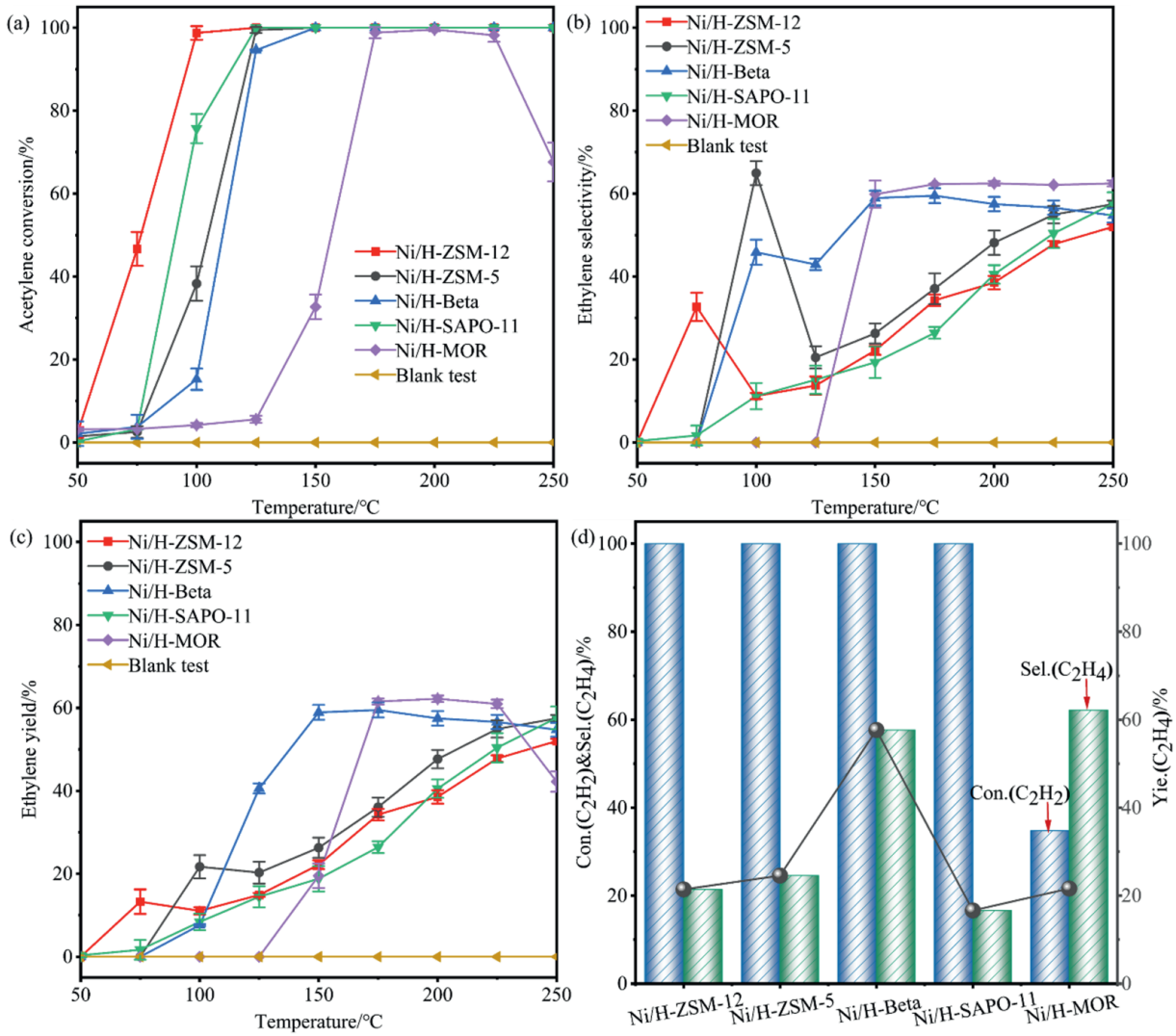


Fig. 9. Hydrogenation performance of the catalyst for acetylene within different temperature ranges: (a) acetylene conversion rate, (b) ethylene selectivity, (c) ethylene yield; (d) catalytic performance at 150 °C.

desorption of physically adsorbed water and surface impurities upon air exposure. Mass loss between 300 °C and 350 °C in the post-stability sample resulted from light hydrocarbon desorption, while loss between 350 °C and 600 °C stemmed from combustion of accumulated green oil and coke deposits. Compared to the freshly reduced sample, the post-stability sample exhibited higher coking rates and greater oligomers accumulation. These deposits impede contact between active metals and reactants, leading to catalyst deactivation. Furthermore, regeneration testing was conducted on the catalyst, revealing that at 550 °C in air, the acetylene conversion rate and ethylene selectivity of the Ni/H-Beta catalyst could be restored to over 95% of their initial levels (Fig. S7). This confirms that deactivation caused by coking is reversible and that the regeneration scheme is effective.

3.2.2. Relationship between structure and catalytic performance of Ni/H-zeolite

In conjunction with *in-situ* DRIFTS results, it can be observed that on the Ni/H-Beta catalyst, as temperature increases, the ν(≡C—H) peak gradually diminishes, the intensity of the σ-bonded $^{*}CH{=}CH_2$ peak progressively increases, and the π-bonded $CH_2{=}CH_2$ group readily desorbs from the Ni/H-Beta catalyst. On the Ni/H-MOR catalyst, however, the ν(≡C—H) peak intensity diminishes more slowly with increasing temperature, whilst the σ-bonded $^{*}CH{=}CH_2$ peak gradually intensifies. This indicates slower C_2H_2 conversion on Ni/H-MOR, but greater C_2H_4 production, consistent with the catalyst performance test results. On Ni/H-ZSM-12, Ni/H-ZSM-5, and Ni/H-SAPO-11 catalysts, the ν(≡C—H) peak intensity diminishes more rapidly, yet C_2H_4 desorption proceeds slowly, consistent with C_2H_4-TPD results. Considering acid properties, Ni electronic states, dispersion, and pore architecture alongside catalyst performance outcomes (Table S5), it is concluded that appropriate micropore and mesopore volumes facilitate reactant molecule access and selective target product formation. Moderately strong acidity promotes reaction progress, though excessive acidity may induce coking; elevated Ni^0 content enhances reaction activation, while high dispersion and small particle size of metallic Ni reduce over-hydrogenation, facilitating ethylene desorption.

3.3. The plausible reaction mechanism

Based on the *in-situ* DRIFTS and other characterization results discussed above, a plausible reaction mechanism for acetylene over the Ni/H-Beta catalyst can be proposed, as illustrated in

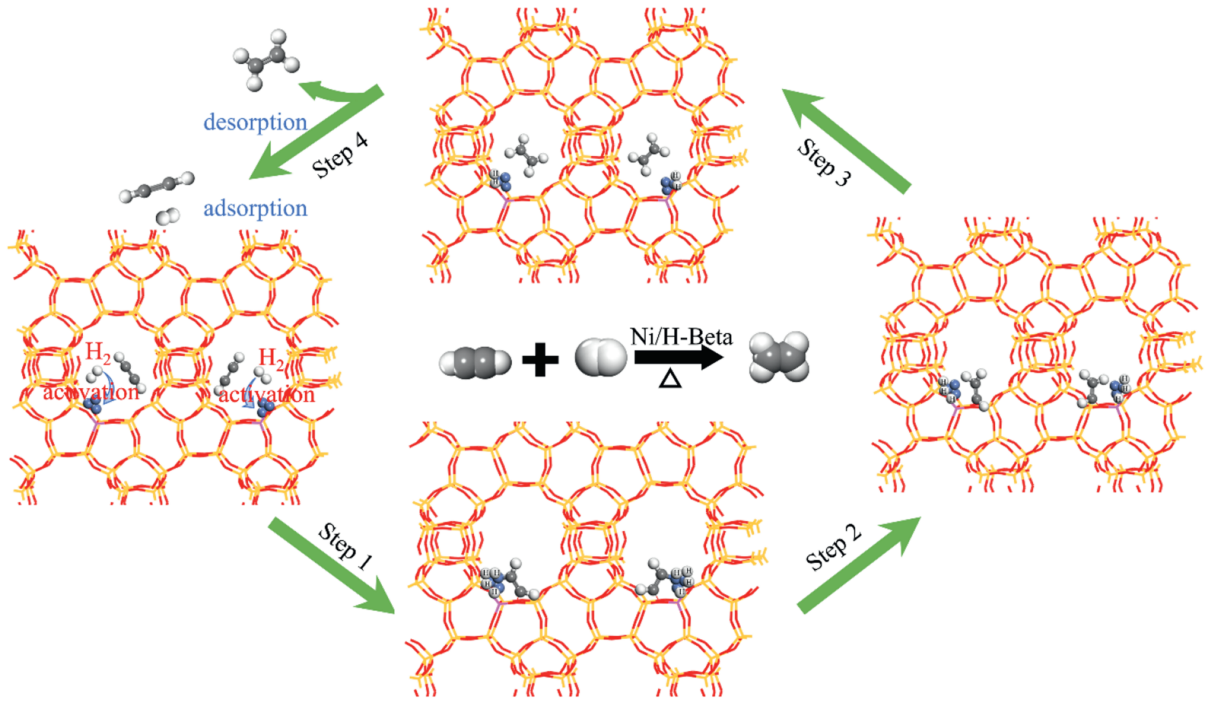


Fig. 10. Mechanism of the selective hydrogenation reaction of acetylene over Ni/H-Beta catalyst. (White: H atoms; gray: C atoms; red: O atoms; pink: Al atoms; yellow: Si atoms; blue: Ni atoms. Step 1: C_2H_2, H_2 adsorption; Step 2: C_2H_2 hydrogenation to $C_2H_3^*$; Step 3: hydrogenation of $C_2H_3^*$ to C_2H_4; Step 4: C_2H_4 desorption.).

Fig. 10. The process initiates with the adsorption and activation of reactant molecules on the catalyst surface (Step 1). Subsequently, the activated hydrogen species (H^*) participate in a hydrogenation step, leading to the formation of a C_2H_3 intermediate (Step 2). This intermediate then combines with additional hydrogen atoms derived from cracking processes to yield C_2H_4 (Step 3). Finally, ethylene (C_2H_4) desorbs from the catalyst into the gas phase as the final product (Step 4).

4. Conclusions

This study systematically compares the performance of nickel catalysts supported on five distinct zeolite topologies (MTW, MFI, BEA, AEL, and MOR) for the selective semi-hydrogenation of acetylene. Among them, the Ni/H-Beta catalyst with BEA topology demonstrated superior catalytic efficiency, achieving complete acetylene conversion with an ethylene yield of 58% at 150 °C. Comprehensive characterization revealed the structural advantages of Ni/H-Beta: its large specific surface area and suitable microporous-mesoporous structure provided an ideal foundation for uniform distribution of active sites, thereby forming highly dispersed nickel species with fine particle size. More importantly, the abundant medium-strong Lewis acid sites in this catalyst effectively modulate the electronic structure of nickel species. This electronic regulation not only facilitates the activation of reactant molecules but also promotes the timely desorption of ethylene products, thereby effectively suppressing over-hydrogenation side reactions. The consistent findings from C_2H_4-TPD and *in-situ* DRIFTS analyses further elucidate the low-temperature reaction advantages of Ni/H-Beta. The moderate ethylene adsorption strength and optimized surface reaction pathway enable the maintenance of high activity even at lower temperatures. By establishing the structure-activity relationship between catalyst characteristics and reaction performance, this work provides a theoretical foundation for understanding the role of zeolite topology in acetylene selective hydrogenation and offers valuable guidance for the rational design of high-efficiency acetylene hydrogenation catalysts.

CRediT Authorship Contribution Statement

Tong Guan: Writing – original draft, Investigation, Formal analysis, Data curation, Conceptualization. Xueming Sun: Validation, Methodology, Investigation. Rongbin Zhang: Writing – review & editing, Funding acquisition. Huaxi Li: Writing – review & editing. Gang Feng: Resources, Project administration, Funding acquisition, Conceptualization. Runping Ye: Writing – review & editing, Validation, Supervision, Resources, Project administration, Funding acquisition, Conceptualization.

Declaration of Competing Interest

The authors declare that they have no known competing financial interests or personal relationships that could have appeared to influence the work reported in this paper.

Acknowledgements

This work was supported by the Natural Science Foundation of Jiangxi Province for Distinguished Young Scholars (20232ACB213001), the National Natural Science Foundation of China (22362022, 52361040), the Thousand Talents Plan of Jiangxi Province (jxsq2023101072), the Natural Science Foundation of Jiangxi Province (20252BAC250133, 20232ACB203004).

Supplementary Material

Supplementary data to this article can be found online at https://doi.org/10.1016/j.cjche.2026.01.009.

References

[1] Y.F. Gao, L. Neal, D. Ding, W. Wu, C. Baroi, A.M. Gaffney, F.X. Li, Recent advances in intensified ethylene production: a review, *ACS Catal.* 9 (9) (2019) 8592–8621.

[2] H.M. Torres Galvis, K.P. de Jong, Catalysts for production of lower olefins from synthesis gas: a review, *ACS Catal.* 3 (9) (2013) 2130–2149.

[3] I.T. Trotuş, T. Zimmermann, F. Schüth, Catalytic reactions of acetylene: a feedstock for the chemical industry revisited, *Chem. Rev.* 114 (3) (2014) 1761–1782.

[4] M. Tejeda-Serrano, M. Mon, B. Ross, F. Gonell, J. Ferrando-Soria, A. Corma, A. Leyva-Pérez, D. Armentano, E. Pardo, Isolated Fe(III)-O sites catalyze the hydrogenation of acetylene in ethylene flows under front-end industrial conditions, *J. Am. Chem. Soc.* 140 (28) (2018) 8827–8832.

[5] X.X. Cao, B.W.L. Jang, J.X. Hu, L. Wang, S.Q. Zhang, Synthetic strategies of supported Pd-based bimetallic catalysts for selective semi-hydrogenation of acetylene: a review and perspectives, *Molecules* 28 (6) (2023) 2572.

[6] L. Qian, J.K. Xue, C. Tao, C. Ma, X.P. Jiang, F.Q. Guo, Effect of demineralization on pyrolysis characteristics of LPS coal based on its chemical structure, *Int. J. Coal Sci. Technol.* 10 (1) (2023) 21.

[7] D. Götz, M. Kuhn, P. Claus, Numerical modelling and performance studies of the original and advanced TEMKIN reactor in laboratory scale testing of industrial egg shell catalysts for the selective hydrogenation of acetylene, *Chem. Eng. Res. Des.* 94 (2015) 594–604.

[8] H. Aeowjaroenlap, K. Chotiwiriyakun, N. Tiensai, W. Tanthapanichakoon, S. Spatenka, A. Cano, Model-based optimization of an acetylene hydrogenation reactor to improve overall ethylene plant economics, *Ind. Eng. Chem. Res.* 57 (30) (2018) 9943–9951.

[9] O. Dehghani, M.R. Rahimpour, A. Shariati, An experimental approach on industrial Pd-Ag supported α-Al_2O_3 catalyst used in acetylene hydrogenation process: mechanism, kinetic and catalyst decay, *Processes* 7 (3) (2019) 136.

[10] E. Alhashmi, G. Ebri, K. Hellgardt, Highly active and stable single-atom cobalt in zeolite for acetylene semihydrogenation, *ACS Catal.* 15 (5) (2025) 4121–4140.

[11] I.G. Donskoy, A.N. Kozlov, M.V. Penzik, D.A. Svishchev, L. Ding, Agglomeration of coal and polyethylene mixtures during fixed-bed co-gasification, *Int. J. Coal Sci. Technol.* 11 (1) (2024) 21.

[12] M. Yang, D. Fan, Y.X. Wei, P. Tian, Z.M. Liu, Recent progress in methanol-to-olefins (MTO) catalysts, *Adv. Mater.* 31 (50) (2019) e1902181.

[13] X.S. Jiajia Ding, Hongxing Liu, Deactivated methanol to olefin catalyst for preparation of SAPO-34 molecular sieve by directing agent method and its application, *Low-Carbon Chem. Chem. Eng.* 49 (8) (2024) 131–137.

[14] H. Lamers, M. Schummer, M. Lucas, M. Rose, Alumina supported iron catalysts for selective acetylene hydrogenation under industrial front-end conditions, *ChemCatChem* 17 (7) (2025) e202401978.

[15] P.N. Kuznetsov, O.Y. Fetisova, L.I. Kuznetsova, B. Avid, B. Purevsuren, Insight into the key kinetic steps in the pyrolysis of coking and non-coking coals, characterization of the pyrolysis products, *Int. J. Coal Sci. Technol.* 10 (1) (2023) 16.

[16] K.S. Kley, J. De Bellis, F. Schüth, Selective hydrogenation of highly concentrated acetylene streams over mechanochemically synthesized PdAg supported catalysts, *Catal. Sci. Technol.* 13 (1) (2023) 119–131.

[17] Q.W. Yang, Z.Y. Sun, B. Shao, J. Hu, Research progress in highly selective hydrogenation of CO_x to light olefins, *Clean Coal Technol* 30 (11) (2024) 1–12.

[18] X.C. Lan, J.G. Chen, T.F. Wang, Recent advances in thermocatalytic acetylene selective hydrogenation, *Chem. Soc. Rev.* 54 (16) (2025) 7654–7705.

[19] Y.C. Chai, W.L. Dai, G.J. Wu, N.J. Guan, L.D. Li, Confinement in a zeolite and zeolite catalysis, *Acc. Chem. Res.* 54 (13) (2021) 2894–2904.

[20] A. Corma, State of the art and future challenges of zeolites as catalysts, *J. Catal.* 216 (1–2) (2003) 298–312.

[21] W. Huang, A. Li, R.F. Lobo, J.G. Chen, Effects of zeolite structures, exchanged cations, and bimetallic formulations on the selective hydrogenation of acetylene over zeolite-supported catalysts, *Catal. Lett.* 130 (3) (2009) 380–385.

[22] M. Sahooli, M.R. Rahimpour, M. Khorram, Fine-tuning synthesis and characterization of mono-sized H-beta zeolite-supported palladium-iridium nanoparticles and application in the selective hydrogenation of acetylene, *Catalysts* 7 (11) (2017) 343.

[23] D.S. Wang, R.P. Ye, C. Zhang, C.K. Jin, Z.H. Lu, M. Shakouri, B.Y. Han, T. Wang, Y.H. Zhang, R.B. Zhang, Y.F. Hu, J. Zhou, G. Feng, Robust Ni_xSn/ZSM-12 catalysts with zeolite as the support and Sn as the promoter for acetylene semihydrogenation, *Energy Fuel.* 37 (17) (2023) 13305–13318.

[24] H. Liu, J.L. Li, X. Liang, H.Y. Ren, H. Yin, L.G. Wang, D. Yang, D.S. Wang, Y.D. Li, Encapsulation of Pd single-atom sites in zeolite for highly efficient semihydrogenation of alkynes, *J. Am. Chem. Soc.* 146 (34) (2024) 24033–24041.

[25] X.F. Shi, B. Zhang, H.W. Chen, J.P. Li, L.B. Li, Organic molecular gate in mordenite for deep removal of acetylene and carbon dioxide from ethylene under humid condition, *Sep. Purif. Technol.* 327 (2023) 124953.

[26] D.X. Wang, J.C. Liu, X.S. Cheng, X. Kang, A.P. Wu, C.G. Tian, H.G. Fu, Trace Pt clusters dispersed on SAPO-11 promoting the synergy of metal sites with acid sites for high-effective hydroisomerization of n-alkanes, *Small Methods* 3 (5) (2019) 1800510.

[27] Q.J. Lin, M.M. Pei, P. Yao, S. Xu, S.H. Xu, S. Liu, H.D. Xu, Y. Dan, Y.Q. Chen, Determining hydrothermal deactivation mechanisms on Cu/SAPO-34 NH_3-SCR catalysts at low- and high-reaction regions: establishing roles of different reaction sites, *Rare Met.* 41 (6) (2022) 1899–1910.

[28] Z.C. Na, L.Y. Pan, H.D. Yao, L. Chen, Y.H. Liu, J.J. Liu, Z.H. Tao, D. Li, W.H. Li, Preparation of core-shell Ni/CeO_2@Al_2O_3 catalyst for selective hydrogenation of acetylene, *Catal. Commun.* 187 (2024) 106860.

[29] S.Z. Zhou, L.H. Kang, Z. Xu, M.Y. Zhu, Catalytic performance and deactivation of Ni/MCM-41 catalyst in the hydrogenation of pure acetylene to ethylene, *RSC Adv.* 10 (4) (2020) 1937–1945.

[30] Y.C. Chai, W.X. Shang, W.J. Li, G.J. Wu, W.L. Dai, N.J. Guan, L.D. Li, Noble metal particles confined in zeolites: synthesis, characterization, and applications, *Adv. Sci.* 6 (16) (2019) 1900299.

[31] G. Sastre, A. Corma, The confinement effect in zeolites, *J. Mol. Catal. Chem.* 305 (1–2) (2009) 3–7.

[32] S. Hu, C. Zhang, M.Y. Wu, R.P. Ye, D.P. Shi, M.J. Li, P. Zhao, R.B. Zhang, G. Feng, Semi-hydrogenation of acetylene to ethylene catalyzed by bimetallic CuNi/ZSM-12 catalysts, *Catalysts* 12 (9) (2022) 1072.

[33] H. Liu, M.Q. Chai, G.X. Pei, X.Y. Liu, L. Li, L.L. Kang, A.Q. Wang, T. Zhang, Effect of IB-metal on Ni/SiO_2 catalyst for selective hydrogenation of acetylene, *Chin. J. Catal.* 41 (7) (2020) 1099–1108.

[34] M.Z. Jian, J.X. Liu, W.X. Li, Hydroxyl improving the activity, selectivity and stability of supported Ni single atoms for selective semi-hydrogenation, *Chem. Sci.* 12 (30) (2021) 10290–10298.

[35] Y.L. Gu, N.Y. Cui, Q.J. Yu, C.Y. Li, Q.K. Cui, Study on the influence of channel structure properties in the dehydration of glycerol to acrolein over H-zeolite catalysts, *Appl. Catal. Gen.* 429 (2012) 9–16.

[36] X.Y. Xing, X. Shi, M.Y. Ruan, Q.C. Wei, Y. Guan, H. Gao, S.Q. Xu, Sulfonic acid functionalized β zeolite as efficient bifunctional solid acid catalysts for the synthesis of 5-hydroxymethylfurfural from cellulose, *Int. J. Biol. Macromol.* 242 (2023) 125037.

[37] K.A. Sun, J. Lu, L.L. Ma, Y. Han, Z.J. Fu, J.C. Ding, A comparative study on the catalytic performance of different types of zeolites for biodiesel production, *Fuel* 158 (2015) 848–854.

[38] Y.Q. Wu, L. Emdadi, S.C. Oh, M. Sakbodin, D.X. Liu, Spatial distribution and catalytic performance of metal–acid sites in Mo/MFI catalysts with tunable meso-/microporous lamellar zeolite structures, *J. Catal.* 323 (2015) 100–111.

[39] Z.X. Qin, S. Zeng, G. Melinte, T. Bučko, M. Badawi, Y.F. Shen, J.P. Gilson, O. Ersen, Y.X. Wei, Z.M. Liu, X.M. Liu, Z.F. Yan, S.T. Xu, V. Valtchev, S. Mintova, Understanding the fundamentals of microporosity upgrading in zeolites: increasing diffusion and catalytic performances, *Adv. Sci.* 8 (17) (2021) 2100001.

[40] R.Z. Liu, Y.K. Bian, W.L. Dai, Qualitative and quantitative analysis of Brønsted and Lewis acid sites in zeolites: a combined probe-assisted ^{1}H MAS NMR and NH_3-TPD investigation, *Chin. J. Struct. Chem.* 43 (4) (2024) 100250.

[41] R. Benrabaa, A. Rubbens, A. Löfberg, R.N. Vannier, Evidence of surface properties by isopropanol decomposition reaction and NH_3-TPD over Ni–Fe spinel nanoparticles prepared *via* hydrothermal route, *ChemistrySelect* 8 (4) (2023) e202204361.

[42] G.Q. Na, W.G. Cui, H.Y. Shi, Z.L. Li, F. Gao, X.Q. Wang, K. Wang, Y. Gao, Y.X. Yang, Z.C. Shen, H.G. Pan, Lewis and Brønsted acid synergistic catalysis in zeolite for boosting hydrogen storage performance of $LiBH_4$, *Rare Met.* 44 (4) (2025) 2379–2392.

[43] M. Romay, D.P. Serrano, J.M. Escola, P. Pizarro, Dry reforming of methane over Ni/MFI catalysts: role of the zeolite support acidity, *Catal. Today* 460 (2025) 115481.

[44] J. McCaig, H. Henry Lamb, Ni-H-beta catalysts for ethylene oligomerization: impact of parent cation on Ni loading, speciation, and siting, *Catalysts* 12 (8) (2022) 824.

[45] C. Sun, P. Beaunier, V. La Parola, L.F. Liotta, P. Da Costa, Ni/CeO_2 nanoparticles promoted by yttrium doping as catalysts for CO_2 methanation, *ACS Appl. Nano Mater.* 3 (12) (2020) 12355–12368.

[46] S.Y. Wang, B. He, R. Tian, C. Sun, R. Dai, X. Li, X. Wu, X. An, X.M. Xie, Ni-hierarchical Beta zeolite catalysts were applied to ethanol steam reforming: effect of sol gel method on loading Ni and the role of hierarchical structure, *Mol. Catal.* 453 (2018) 64–73.

[47] C.Q. Sui, H. Ma, F. Huang, M.L. Wang, X.B. Cai, J.Y. Diao, P.J. Ren, X.D. Wen, L. Jin, G.Q. Wang, D. Ma, H.Y. Liu, Fully exposed nickel clusters for semihydrogenation of acetylene, *ACS Catal.* 14 (19) (2024) 14689–14695.

[48] Y. Zeng, M.Q. Xia, F.J. Gao, C.K. Zhou, X.Y. Cheng, L.W. Liu, L. Jiao, Q. Wu, X.Z. Wang, L.J. Yang, Y.N. Fan, Z. Hu, Impact of Pd single-site coordination structure on catalytic performance for semihydrogenation of acetylene, *Nano Res.* 17 (9) (2024) 8243–8249.

[49] X.H. Ge, Y.D. Jing, N.N. Fei, K.L. Yan, Y.J. Liang, Y.Q. Cao, J. Zhang, G. Qian, L.N. Li, H. Jiang, X.G. Zhou, W.K. Yuan, X.Z. Duan, Embedding single Pd atoms on NiGa intermetallic surfaces for efficient and selective alkyne hydrogenation, *Angew. Chem. Int. Ed.* 63 (43) (2024) e202410979.

[50] K. Shimura, S. Yoshida, H. Oikawa, T. Fujitani, Impacts of Ni-loading method on the structure and the catalytic activity of NiO/SiO_2-Al_2O_3 for ethylene oligomerization, *Catalysts* 13 (9) (2023) 1303.

[51] B.A. Fu, A.J. McCue, Y.N. Liu, S.X. Weng, Y.F. Song, Y.F. He, J.T. Feng, D.Q. Li, Highly selective and stable isolated non-noble metal atom catalysts for selective hydrogenation of acetylene, *ACS Catal.* 12 (1) (2022) 607–615.

[52] W. Huang, J.R. McCormick, R.F. Lobo, J.G. Chen, Selective hydrogenation of acetylene in the presence of ethylene on zeolite-supported bimetallic catalysts, *J. Catal.* 246 (1) (2007) 40–51.

[53] H.R. Zhou, B.H. Ye, H.G. Fu, X.L. Wei, Z.K. Ma, H.N. Yin, Y.Y. Yuan, Y. Liu, Alumina-supported palladium modified by zeolite Socony Mobil-5 for highly efficient selective hydrogenation of acetylene in excess ethylene, *J. Colloid Interface Sci.* 696 (2025) 137907.
[54] X. Li, X.N. Li, Efficient electronic state regulation engineering on Pd single atom by the defect engineering of the BN support for acetylene semi-hydrogenation, *Mol. Catal.* 564 (2024) 114324.
[55] J.Y. Zhao, L. He, J.D. Yu, Y.Z. Shi, R.R. Miao, Q.Q. Guan, P. Ning, Preparation of MCM-41 supported nickel NPs for the high-efficiency semi-hydrogenation of acetylene, *New J. Chem.* 45 (2) (2021) 1054–1062.
[56] W. Huang, W. Pyrz, R.F. Lobo, J.G. Chen, Selective hydrogenation of acetylene in the presence of ethylene on K^+-β-zeolite supported Pd and PdAg catalysts, *Appl. Catal. Gen.* 333 (2) (2007) 254–263.
[57] Y.J. Chen, J.X. Chen, Selective hydrogenation of acetylene on SiO_2 supported Ni-In bimetallic catalysts: promotional effect of, *Appl. Surf. Sci.* 387 (2016) 16–27.
[58] L. Wang, F.X. Li, Y.J. Chen, J.X. Chen, Selective hydrogenation of acetylene on SiO_2-supported Ni-Ga alloy and intermetallic compound, *J. Energy Chem.* 29 (2019) 40–49.
[59] B.I. Mosqueda-Jiménez, A. Jentys, K. Seshan, J.A. Lercher, Structure-activity relations for Ni-containing zeolites during NO reduction I. Influence of acid sites, *J. Catal.* 218 (2) (2003) 348–353.
[60] R. Cuevas-García, J.G. Téllez-Romero, J. Ramírez, P. Sarabia-Bañuelos, I. Puente-Lee, C. Salcedo-Luna, S. Hernández-González, V.A. Nolasco-Arizmendi, Effect of the preparation method on particle size and reaction selectivity on naphthalene hydrogenation over Ni/H-MOR catalysts, *Catal. Today* 360 (2021) 63–71.